PROCEEDINGS, 51st Workshop on Geothermal Reservoir Engineering
Stanford University, Stanford, California, February 9-11, 2026
SGP-TR-230

A Multiscale Thermo-Mechanical Framework for Geothermal Applications

Shabnam J. Semnani* and Ruofan Wu

University of California San Diego, CA, USA 92093

*ssemnani@ucsd.edu

Keywords: Multi-scale, homogenization, anisotropy, thermo-mechanical coupling

ABSTRACT

Natural rocks in geothermal energy reservoir are heterogeneous and consist of fractures, solid and fluid phases that form complex structures at multiple scales. Explicit incorporation of multiple scales of fractures and heterogeneities into large-scale tightly coupled models is impractical and would cause tremendous computational costs. Therefore, efficient multi-scale and multi-physics strategies are necessary for capturing sub-grid-scale processes and their impacts on macroscopic behavior. In this work, we present a multiscale framework for coupled thermo-mechanical behavior of rocks in geothermal reservoir. The proposed approach allows for separate micro-constitutive laws, which provides an efficient way of capturing both large- and small-scale processes. The performance of the modeling framework in simulation of geothermal energy reservoir is demonstrated through numerical examples.

1. INTRODUCTION

Enhanced geothermal systems (EGSs) are underground reservoirs where fluid can flow through the hot rocks, absorbing heat from the rocks that can be brought to the surface for use in a variety of applications (Tester et al., 2006). The importance of geothermal systems is increasing due to their energy security and low-carbon emissions compared with many other renewables. However, EGS requires reliable prediction and management of subsurface behavior. Unlike many engineered energy systems, EGS performance is controlled by coupled processes in a heterogeneous geological medium where heat transport occurs through fractures and pores which can evolve under changing thermo-mechanical conditions. Predicting the performance of EGS systems requires advanced modeling approaches that can link rock properties and microstructure to field-scale responses.

In order to ensure the long term EGS stability and serviceability during injection and production of fluid wells, factors such as heat transfer, stress response, and thermo-mechanical (TM) coupling must be studied thoroughly. TM coupling refers to the interaction between temperature and displacement fields: temperature changes cause deformation through thermal expansion or contraction and potentially, deformation alters conductivity properties and heat flow. In geothermal applications, injection of cooler fluid into hot rock commonly induces thermal contraction near injection wells, producing thermal stress concentration that can open or close fractures (Rathnaweera et al., 2020; Zhou et al., 2024; Parisio et al., 2019). Similarly, deformation and stress alter fracture apertures and contact conditions, ultimately influencing heat extraction efficiency. Coupled TM modelling is therefore central to predicting reservoir performance and risk. Reviews of fractured rock modeling in geothermal applications commonly identify TM coupling as essential for predicting fracture network evolution and long-term performance (Vaezi et al., 2025). From a modeling standpoint, TM coupling typically enters through thermoelastic or thermoplastic constitutive relations, where temperature changes produce thermal strains that affect the total stresses (Jiménez-Camargo et al., 2025). This can further promote or suppress fracture opening and influence the mechanical interaction among fracture planes (Salimzadeh et al., 2018; Pandey et al., 2017; Zhou et al., 2024; Aliyu, 2025).

EGS performance is controlled by strongly coupled thermo-mechanical processes that act across spatial scales: from microscopic mineral fabric to geothermal reservoir. Natural soils and rocks are typically anisotropic with direction-dependent thermal conductivity, mechanical properties, and thermal expansion. In geological settings, anisotropy commonly arises from fabric, layering, mineral orientation, and fractures, where bedding planes create strong contrasts between in-plane and cross-plane transport and deformation mechanisms (Abuel-Naga & Bergado, 2005). Shales are common examples of transversely isotropic rocks, where anisotropy arises in the bedding plane normal direction (Kim et al., 2012). Thermal anisotropy is also widely observed in clay-rich and layered formations, where thermal conductivity parallel to bedding planes can differ significantly from that normal to bedding, affecting predicted temperature fields (Davis et al., 2007). Mechanical anisotropy similarly impacts wellbore stability, fracture growth, and stress evolution (Choo et al., 2021). Recent studies emphasize the possibility of scale dependence in heterogeneous geomaterials, which motivates homogenization and upscaling approaches for field-scale simulations (Wu et al., 2021).

A central challenge in modeling anisotropy is that fully anisotropic constitutive descriptions are often difficult to derive and involve intensive computational time. Existing anisotropic modeling approaches can be broadly grouped into either thermal or mechanical. Thermal anisotropic models used in the literature have employed the generalized Fourier's law to form a second-order conductivity tensor, enabling representation of transversely isotropic, orthotropic, and fully anisotropic conduction (Wang et al., 2021; Kim et al., 2012), homogenization and upscaling methods that compute effective conductivities from multi-phase microstructures in composites (Giraud et al., 2007; Giraud et al., 2008). Mechanical anisotropy is often captured with anisotropic elastic, path- or rate-dependent response considering strength criteria that embed plane of weakness which are widely observed for layered sedimentary rocks (Choo et al., 2021; Semnani & White, 2020). Additional anisotropic models such as critical-state-based models incorporates rotated yield surfaces and rotational hardening rules (Wheeler et al., 2003; Dafalias et al., 2006; Rezania & Dejaloud, 2021; Semnani et al., 2016). Viscous extensions further combine anisotropy with rate dependence to represent creep and time-dependent deformation (Yin et al., 2010). Microstructure-based approaches for anisotropic clayey rocks employ multistep homogenization to determine macroscopic elastic tensors and yield behavior (Chen et al., 2023). Thermo-mechanical anisotropy models typically require both anisotropic thermal and mechanical responses. Classical thermo-elasticity generalizes the constitutive relation by introducing a directional thermal expansion tensor, as well as an anisotropic stiffness, enabling directional thermal stress development (Cooper & Simmons, 1977).

While rock microstructure determines the macroscopic anisotropic thermo-mechanical behavior of these materials, directly resolving microstructure at the microscale is computationally infeasible. Homogenization techniques provide a systematic approach to bridge these scales by deriving macroscopic constitutive behavior from representative microstructures while preserving coupling between thermal and mechanical fields. This work is motivated by the need for reliable coupled TM predictions in EGS performance and risk assessment by providing a methodology to embed microstructural anisotropy into continuum-scale TM simulations. We develop a multiscale thermo-mechanical homogenization framework tailored to layered rocks, in which anisotropic thermo-mechanical response is naturally captured due to the layered microstructure. We develop a material update algorithm based on the proposed homogenization scheme and implement it within the Finite Element framework to perform boundary value simulations. The paper is organized as follows: Section 2 discusses the technical details of the homogenization framework for thermo-mechanical coupling and the material point update algorithm. Section 3 includes the corresponding finite element method (FEM) implementations. Section 4 is dedicated to numerical examples for verifying the homogenization model against high-fidelity FEM simulations, as well as a wellbore boundary value problem to demonstrate the applicability of the proposed approach in practical geological settings.

2. MULTI-SCALE MODELING FRAMEWORK

In the following sections, we present a multiscale thermo-mechanical homogenization framework for layered materials. The approach combines microscale boundary-value problems defined on periodic unit cells with macroscopic balance laws for energy and linear momentum. The methodology produces homogenized stress and heat flux, as well as effective macroscopic stiffness and conductivity tensors to be implemented in a macroscopic thermo-mechanical finite element framework. Furthermore, the proposed approach allows us to incorporate path- and rate-dependent behaviors of the rock materials.

2.1 Asymptotic Homogenization

Consider a macroscopic body Ω with a microstructure represented by a spatially periodic unit cell Y. The unit cell is composed of repeating parallel layers Y_m with index $m \in L = \{1,2,\dots,M\}$. The material is Y-periodic in the direction normal to the layers, $\mathbf{n}$, resulting in a unidirectional microstructure. We assume that the displacement field is continuous within each layer Y_m. Following the asymptotic homogenization theory a macroscopic coordinate, $\mathbf{x}$, and a microscopic coordinate, $\mathbf{y}$ are considered. We define L and l to be the macroscopic and microscopic characteristic length scales and define the period ϵ of the unit cell as

$$\epsilon = \frac{l}{L}, \quad \epsilon \ll 1 \tag{1}$$

with the two coordinate systems related as

$$y = x/\epsilon \tag{2}$$

Due to the unidirectional periodicity of the unit cell, a scalar microscopic coordinate y is defined as

$$y = \mathbf{y} \cdot \mathbf{n} = \frac{1}{\epsilon}(\mathbf{x} \cdot \mathbf{n}) \tag{3}$$

It is assumed that the two scales, $\mathbf{x}$ and y are clearly separated and all material properties are Y-periodic fields. The microstructure at each integration point is assumed to be periodic. Accordingly, the material model developed here is applied at an integration point within a finite element solver. We note that the total derivative with respect to $\mathbf{x}$ can be computed as

$$\frac{d}{d\mathbf{x}} = \frac{\partial}{\partial \mathbf{x}} + \frac{1}{\epsilon}\frac{\partial}{\partial \mathbf{y}} \tag{4}$$

Similarly, divergence of a continuous second order tensor $\boldsymbol{\sigma}$ can be written as

$$\nabla \cdot \dot{\boldsymbol{\sigma}} = \nabla_x \cdot \dot{\boldsymbol{\sigma}} + \frac{1}{\epsilon}\nabla_y \cdot \dot{\boldsymbol{\sigma}} \tag{5}$$

where

$$(\nabla_x \cdot \dot{\boldsymbol{\sigma}})_{ij} = \frac{\partial \dot{\sigma}_{ij}}{\partial x_j} \quad \text{and} \quad \left(\nabla_y \cdot \dot{\boldsymbol{\sigma}}\right)_{ij} = \frac{\partial \dot{\sigma}_{ij}}{\partial y}\, n_j \tag{6}$$

2.2 Governing Equations

Let us denote by $\mathbf{u}(\mathbf{x}, y)$ the displacement field and $T(\mathbf{x}, y)$ the temperature field where both unknown fields are a function of the macroscopic and microscopic coordinates. Because we are interested in nonlinear material behavior, we choose to work with the rate form of the momentum equation to derive the homogenized model. Consider the balance of linear momentum as:

$$\nabla \cdot \dot{\boldsymbol{\sigma}} + \dot{\mathbf{b}} = \mathbf{0} \tag{7}$$

$$\nabla \cdot \left[\mathbf{C} \colon \left(\dot{\boldsymbol{\varepsilon}} - \boldsymbol{\alpha}_{\mathbf{s}} \dot{T} \right) \right] + \dot{\mathbf{b}} = \mathbf{0} \tag{8}$$

in which $\mathbf{C}$ is the stiffness tangent, $\boldsymbol{\alpha}_{\mathbf{s}}$ is the thermal expansion matrix, and $\mathbf{b}$ is the body force. The energy balance equation is

$$(\rho c)_{\text{eff}} \dot{T} + \nabla \cdot \mathbf{q}_{\mathrm{T}} = r_{\mathrm{T}}$$

$$\mathbf{q}_{\mathrm{T}} = \boldsymbol{\kappa}_{T} \cdot \nabla T \tag{9}$$

where ρ and c denote the mass density and specific heat capacity of the mixture, $\mathbf{q}_{\mathrm{T}}$ denotes heat flux, $\boldsymbol{\kappa}_{T}$ is the thermal conductivity matrix and r_{T} is the energy source term. following the asymptotic homogenization theory, the unknown displacement and temperature fields can be represented by a truncated power series of ϵ as

$$\begin{aligned} \mathbf{u}(\mathbf{x}, y) &= \mathrm{u}^{(0)} + \epsilon \mathbf{u}^{(1)} + \epsilon^{2} \mathbf{u}^{(2)} + \cdots \\ T(\mathbf{x}, y) &= T^{(0)} + \epsilon T^{(1)} + \epsilon^{2} T^{(2)} + \cdots \end{aligned} \tag{10}$$

We have

$$\dot{\boldsymbol{\sigma}} = \epsilon^{-1} \dot{\boldsymbol{\sigma}}^{(-1)} + \epsilon^{0} \dot{\boldsymbol{\sigma}}^{(0)} + \epsilon^{1} \dot{\boldsymbol{\sigma}}^{(1)} + \cdots$$

$$\mathbf{q}_{\mathrm{T}} = \epsilon^{-1} \mathbf{q}_{\mathrm{T}}^{(-1)} + \epsilon^{0} \mathbf{q}_{\mathrm{T}}^{(0)} + \epsilon^{1} \mathbf{q}_{\mathrm{T}}^{(1)} + \cdots \tag{11}$$

By replacing Equation (11) in Equations (7) and (9) and setting orders of ϵ^{-2}, ϵ^{-1} and ϵ^{0} to zero, we obtain for the balance of momentum:

$$\nabla_{y} \cdot \dot{\boldsymbol{\sigma}}^{(-1)} = 0 \tag{12a}$$

$$\nabla_{x} \cdot \dot{\boldsymbol{\sigma}}^{(-1)} + \nabla_{y} \cdot \dot{\boldsymbol{\sigma}}^{(0)} = 0 \tag{12b}$$

$$\nabla_{x} \cdot \dot{\boldsymbol{\sigma}}^{(0)} + \nabla_{y} \cdot \dot{\boldsymbol{\sigma}}^{(1)} = 0 \tag{12c}$$

For the balance of energy, we obtain:

$$\nabla_{y} \cdot \mathbf{q}_{\mathrm{T}}^{(-1)} = 0 \tag{13a}$$

$$\nabla_{x} \cdot \mathbf{q}_{\mathrm{T}}^{(-1)} + \nabla_{y} \cdot \mathbf{q}_{\mathrm{T}}^{(0)} = 0 \tag{13b}$$

$$\nabla_{x} \cdot \mathbf{q}_{\mathrm{T}}^{(0)} + \nabla_{y} \cdot \mathbf{q}_{\mathrm{T}}^{(1)} + (\rho c)_{\text{eff}} \dot{T}^{(0)} = r_{\mathrm{T}} \tag{13c}$$

From Equations (12a) and (13a) we have

$$\dot{\mathbf{u}}^{(0)} = \dot{\mathbf{u}}^{(0)}(\mathbf{x}), \quad \frac{\partial \dot{\mathbf{u}}^{(0)}}{\partial \mathbf{y}} = 0, \quad \dot{\boldsymbol{\sigma}}^{(-1)} = 0 \tag{14}$$

$$T^{(0)} = T^{(0)}(\mathbf{x}), \quad \frac{\partial T(0)}{\partial \mathbf{y}} = 0, \quad \mathbf{q}_{\mathrm{T}}^{(-1)} = 0 \tag{15}$$

Here, $\mathbf{u}^{(0)}(\mathbf{x})$ and $T^{(0)}(\mathbf{x})$ represent the macroscopic component of the displacement and temperature fields, which are only a function of the macroscopic coordinate. In contrast, $\mathbf{u}^{(1)}(\mathbf{x}, y)$ and $T^{(1)}(\mathbf{x}, y)$ represent the microscopic displacement and temperature fluctuations, which vary quasi-periodically across unit cells. Using Equation (14) in Equation (12b) leads to the microscopic momentum balance:

$$\nabla_{y} \cdot \dot{\boldsymbol{\sigma}}^{(0)} = 0 \tag{16}$$

Therefore, $\dot{\boldsymbol{\sigma}}^{(0)} \cdot \mathbf{n} = \dot{\mathbf{t}}(\mathbf{x})$ is constant in unit cell *Y*. Similarly, using Equation (15) in Equation (13b) leads to the microscopic energy conservation:

$$\nabla_{y} \cdot \mathbf{q}_{\mathrm{T}}^{(0)} = 0 \tag{17}$$

Therefore, $\mathbf{q}_{\mathrm{T}}^{(0)} \cdot \mathbf{n} = \mathrm{f}_{T}(\mathbf{x})$ is constant in unit cell *Y*. Here, $\mathbf{t}(\mathbf{x})$ denotes the traction vector resulting from stresses acting in the bedding normal direction, which must be continuous in all layers to satisfy unit cell equilibrium. Similarly, $f_{\mathrm{T}}(\mathbf{x})$ denotes the heat flux vector that must also be in equilibrium in the bedding normal direction.

Let us define the averaging operator $\langle \bullet \rangle = \frac{1}{|Y|} \int_{Y} (\,\bullet) \mathrm{d}y$. Applying the averaging operator to Equation (12c) yields the macroscopic balance of momentum as

$$\begin{gathered}\frac{1}{|Y|}\left[\int_Y \nabla_x\cdot\dot{\boldsymbol{\sigma}}^{(0)}\mathrm{d}y+\int_Y \nabla_y\cdot\dot{\boldsymbol{\sigma}}^{(1)}\mathrm{d}y+\int_Y \dot{\mathbf{b}}\ \mathrm{d}y\right]=0\\ \frac{1}{|Y|}\left[\nabla_x\cdot\int_Y \dot{\boldsymbol{\sigma}}^{(0)}\,\mathrm{d}y+\int_{\Gamma_Y}\dot{\boldsymbol{\sigma}}^{(1)}\cdot\mathbf{n}\cdot\mathrm{d}\Gamma+\int_Y \dot{\mathbf{b}}\ \mathrm{d}y\right]=0\\ \nabla_x\cdot\left\langle\dot{\boldsymbol{\sigma}}^{(0)}\right\rangle+\langle\dot{\mathbf{b}}\rangle=0\\ \nabla_x\cdot\dot{\boldsymbol{\Sigma}}+\dot{\mathbf{B}}=0\end{gathered}\tag{18}$$

Similarly, applying the averaging operator to Equation (13c) gives the macroscopic balance of energy equation as

$$\begin{gathered}\frac{1}{|Y|}\left[\int_Y \nabla_x\cdot\mathbf{q}_{\mathrm{T}}^{(0)}\mathrm{d}y+\int_Y(\rho c)_{\mathrm{eff}}\dot{T}^{(0)}\mathrm{d}y\right]=\frac{1}{|Y|}\int_Y r_{\mathrm{T}}\,\mathrm{d}y\\ \frac{1}{|Y|}\left[\nabla_x\cdot\int_Y\mathbf{q}_{\mathrm{T}}^{(0)}\,\mathrm{d}y+\dot{T}^{(0)}\int_Y(\rho c)_{\mathrm{eff}}\,\mathrm{d}y\right]=\frac{1}{|Y|}\int_Y r_{\mathrm{T}}\,\mathrm{d}y\\ \nabla_x\cdot\left\langle\mathbf{q}_{\mathrm{T}}^{(0)}\right\rangle+\langle(\rho c)_{\mathrm{eff}}\rangle\dot{T}^{(0)}=R_{\mathrm{T}}\\ \nabla_x\cdot\mathbf{Q}_{\mathrm{T}}+(\rho c)_{\mathrm{eff}}\dot{T}^{(0)}=R_{\mathrm{T}}\end{gathered}\tag{19}$$

The displacement, temperature, strain and temperature gradient fields can be additively decomposed using two scale approximations as

$$\mathbf{u}=\mathbf{u}^{(0)}+\epsilon\mathbf{u}^{(1)}\tag{20}$$

$$T=T^{(0)}+\epsilon T^{(1)}\tag{21}$$

$$\boldsymbol{\varepsilon}=\boldsymbol{\varepsilon}_m=\nabla_x^s\mathbf{u}^{(0)}+\nabla_y^s\mathbf{u}^{(1)}=\mathbf{E}(\mathbf{x})+\mathbf{e}\tag{22}$$

$$\nabla T=\nabla T_m=\nabla_x T^{(0)}+\nabla_y T^{(1)}=\mathbf{G}_{\mathrm{T}}(x)+g_T\tag{23}$$

The strain and temperature gradient fields are potentially discontinuous at the layer interfaces, despite the continuity of displacement and temperature fields throughout the unit cell. Since $u^{(1)}$ and $T^{(1)}$ are periodic in Y, the following compatibility conditions must be satisfied:

$$\sum_{m\in L}\int_{Y_m}\frac{\partial\mathbf{u}^{(1)}}{\partial y}\,\mathrm{d}y=0\tag{24}$$

$$\sum_{m\in L}\int_{Y_m}\frac{\partial T^{(1)}}{\partial y}\,\mathrm{d}y=0\tag{25}$$

where m denotes the m-th layer. We also define the microscopic displacement gradient vectors and microscopic temperature gradient vectors of the layers as

$$\mathbf{v}_m=\frac{\partial\mathbf{u}_m^{(1)}}{\partial y},\quad\boldsymbol{\varepsilon}_m=\mathbf{E}+\mathbf{v}_m\overset{s}{\otimes}\mathbf{n}\tag{26}$$

$$g_{\mathrm{T}_m}=\frac{\partial T_m^{(1)}}{\partial y},\quad\nabla T_m=\mathbf{G}_{\mathrm{T}}+g_{\mathrm{T}_m}\mathbf{n}\tag{27}$$

By denoting ϕ_m to be the volume fraction of layer m, with $\sum_{m\in L}\phi_m=1$, Equation (24) and (25) become

$$\sum_{m\in L}\phi_m\,\mathbf{v}_m=\mathbf{0}\tag{28}$$

$$\sum_{m\in L}\phi_m\,g_{\mathrm{T}_m}=0\tag{29}$$

The micro-scale balance equations to be satisfied for each layer are

$$\boldsymbol{\sigma}_m.\boldsymbol{n}=\boldsymbol{t}_0(\boldsymbol{x})\tag{30}$$

$$\mathbf{q}_{\mathrm{T}_m}.\boldsymbol{n}=\boldsymbol{f}_T(\boldsymbol{x})\tag{31}$$

where $\boldsymbol{\sigma}_m$ and $\mathbf{q}_{\mathrm{T}_m}$denote the stress tensor and heat flux within each layer, respectively. Note that the particular models chosen for the layers do not impact the overall homogenization algorithm.

2.3 Solution to the Micro-scale Problem

We use brackets $\{.\}$ to denote a second order tensor that has been converted to a vector form. Let

$$\mathbf{B_1} = \begin{bmatrix} n_1 & 0 & 0 \\ 0 & n_2 & 0 \\ 0 & 0 & n_3 \\ 0 & n_3 & n_2 \\ n_3 & 0 & n_1 \\ n_2 & n_1 & 0 \end{bmatrix}, \quad \mathbf{B_2} = \begin{bmatrix} n_1 \\ n_2 \\ n_3 \end{bmatrix} \tag{32}$$

The strain and temperature gradient of the layers are defined in vector form as

$$\begin{aligned} \{\boldsymbol{\varepsilon}_{m}\} &= \{\mathbf{E}\} + \mathbf{B_1}\mathbf{v}_m \\ \nabla T_m &= \mathbf{G}_\mathrm{T} + \mathbf{B_2} g_{\mathrm{T}_m} \end{aligned} \tag{33}$$

For the case of a bi-layer medium with two layers A and B, applying the microscopic continuity and periodicity conditions gives the following residual and unknown vectors

$$\mathbf{R}(\mathbf{X}) = \begin{bmatrix} \mathbf{B_1}^\top\{\boldsymbol{\sigma}_A\} - \mathbf{t} \\ \mathbf{B_1}^\top\{\boldsymbol{\sigma}_B\} - \mathbf{t} \\ \phi_A\mathbf{v}_A + \phi_B\mathbf{v}_B \\ \mathbf{B_2}^\top\mathbf{q}_{\mathrm{T}_A} - f_\mathrm{T} \\ \mathbf{B_2}^\top\mathbf{q}_{\mathrm{T}_B} - f_\mathrm{T} \\ \phi_A g_{\mathrm{T}_A} + \phi_B g_{\mathrm{T}_B} \end{bmatrix} = \mathbf{0} \quad \text{with} \quad \mathbf{X} = \begin{bmatrix} \mathbf{v}_A \\ \mathbf{v}_B \\ \mathbf{t} \\ g_{\mathrm{T}_A} \\ g_{\mathrm{T}_B} \\ f_\mathrm{T} \end{bmatrix} \tag{34}$$

The Jacobian matrix is derived by linearization of the nonlinear residual vector as

$$\boldsymbol{\mathcal{J}} = \frac{\partial\mathbf{R}}{\partial\mathbf{X}} = \begin{bmatrix} \mathbf{B_1}^\top\mathbf{C}_A\mathbf{B_1} & & \mathbf{-1} & & & \\ & \mathbf{B_1}^\top\mathbf{C}_B\mathbf{B_1} & \mathbf{-1} & & & \\ \phi_A\mathbf{1} & \phi_B\mathbf{1} & & & & \\ & & & \mathbf{B_2}^\top\boldsymbol{\kappa}_{\mathrm{T}_A}\mathbf{B_2} & & -1 \\ & & & & \mathbf{B_2}^\top\boldsymbol{\kappa}_{\mathrm{T}_B}\mathbf{B_2} & -1 \\ & & & \phi_A & \phi_B & \end{bmatrix} \tag{35}$$

At convergence, we calculate the macroscopic stress tensor, $\boldsymbol{\Sigma}$, and the macroscopic heat flux tensor, $\mathbf{Q}_\mathrm{T}$, which are defined as the volume averages of the microscopic stress and heat flux tensors in each layer, respectively,

$$\boldsymbol{\Sigma} = \textstyle\sum_{m\in L} \phi_m\, \boldsymbol{\sigma}_m, \quad \mathbf{Q}_\mathrm{T} = \textstyle\sum_{m\in L} \phi_m\, \mathbf{q}_{\mathrm{T}_m} \tag{36}$$

Letting $\boldsymbol{\mathcal{G}} = \boldsymbol{\mathcal{J}}^{-1}$, the homogenized consistent tangent operator is calculated as

$$\bar{\mathbf{C}} = \frac{\partial\{\boldsymbol{\Sigma}\}}{\partial\{\mathbf{E}\}} = \textstyle\sum_{m\in L} \phi_m\mathbf{C}_m - \sum_{m\in L}\sum_{n\in L} \phi_m\boldsymbol{C}_m\mathbf{B_1}\boldsymbol{\mathcal{G}}_{mn}^{11}\,\mathbf{B_1}^\top\mathbf{C}_n \tag{37}$$

where $\boldsymbol{\mathcal{G}}_{mn}^{11}$ represents the upperleft sub-block of matrix $\boldsymbol{\mathcal{G}}$, whose row and column indices correspond to the residual equations for layer m and n. Similarly, the homogenized thermal conductivity tensor is obtained as:

$$\bar{\mathbf{K}}_\mathrm{T} = \frac{\partial\mathbf{Q}_\mathrm{T}}{\partial\mathbf{G}_\mathrm{T}} = \textstyle\sum_{m\in L} \phi_m\boldsymbol{\kappa}_{\mathrm{T}_m} - \sum_{m\in L}\sum_{n\in L} \phi_m\boldsymbol{\kappa}_{\mathrm{T}_m}\mathbf{B_2}\boldsymbol{\mathcal{G}}_{mn}^{33}\,\mathbf{B_2}^\top\boldsymbol{\kappa}_{\mathrm{T}_n} \tag{38}$$

where $\boldsymbol{\kappa}_{\mathrm{T}_m}$ denotes the thermal conductivity matrix of layer m and $\boldsymbol{\mathcal{G}}_{mn}^{33}$ represents the lower-right sub-block of matrix $\boldsymbol{\mathcal{G}}$.

3. FINITE ELEMENT FORMULATION

By decomposing the boundary Γ of the problem domain Ω into regions where essential and natural boundary conditions are specified, the boundary conditions are given as

$$\begin{aligned} \mathbf{u} &= \bar{\mathbf{u}} && \text{on } \Gamma_\mathbf{u} \\ \mathbf{n}\cdot\boldsymbol{\sigma} &= \bar{\mathbf{t}} && \text{on } \Gamma_\mathbf{t} \\ T^{(0)} &= \bar{T} && \text{on } \Gamma_T \\ \mathbf{Q}_\mathrm{T}\,.\,\bar{\boldsymbol{n}} &= \bar{q}_\mathrm{T} && \text{on } \Gamma_{q_\mathrm{T}}. \end{aligned}$$

$$[\![\mathbf{Q}_\mathrm{T}\,.\,\boldsymbol{n}]\!] = 0$$

$$T^{(0)}(\boldsymbol{x}, y, 0) = T_0(\boldsymbol{x}, y) \tag{39}$$

where $\varGamma_{\mathbf{u}}$ is the solid displacement boundary, $\varGamma_{\mathbf{t}}$ is the solid traction boundary, $\varGamma_T$ is the temperature boundary, and $\varGamma_{q_{\mathrm{T}}}$ is the heat flux boundary. Finally, for all $\mathbf{x} \in \varOmega$ initial conditions at $t = 0$ are given as

$$\mathbf{u}(\mathbf{x}, t = 0) = \mathbf{u}_0, \quad T(\mathbf{x}, t = 0) = T_0 \tag{40}$$

We consider the spaces of trial functions defined as

$$\begin{aligned} \mathcal{U} &= \{\mathbf{u}: \varOmega \to R^3 \mid u_i \in H^1, \mathbf{u} = \bar{\mathbf{u}} \text{ on } \varGamma_{\mathbf{u}}\} \\ \mathcal{T} &= \{T: \varOmega \to R^3 \mid T \in H^1, T = \bar{T} \text{ on } \varGamma_T\} \end{aligned} \tag{41}$$

where H^1 denotes a Sobolev space of degree one. We also define the corresponding spaces of testing functions

$$\begin{aligned} \mathcal{U}^* &= \{\boldsymbol{\eta}: \varOmega \to R^3 \mid \eta_i \in H^1, \boldsymbol{\eta} = \mathbf{0} \text{ on } \varGamma_{\mathbf{u}}\} \\ \mathcal{T}^* &= \{\phi: \varOmega \to R^3 \mid \phi \in H^1, \phi = 0 \text{ on } \varGamma_T\} \end{aligned} \tag{42}$$

Defining $\dot{\boldsymbol{\sigma}}'' = \mathbb{C}: \dot{\boldsymbol{\varepsilon}}$ and $\boldsymbol{\beta} = \mathbb{C}: \boldsymbol{\alpha}_{\mathbf{s}}$, the weak form of the problem is then to find $\{\mathbf{u}, T\} \in \mathcal{U} \times \mathcal{T}$ such that for all $\{\boldsymbol{\eta}, \phi\} \in \mathcal{U}^* \times \mathcal{T}^*$,

$$\begin{aligned} &\int_\varOmega \nabla^{\mathrm{s}} \boldsymbol{\eta}: \dot{\boldsymbol{\sigma}}'' \mathrm{d}\varOmega - \int_\varOmega \nabla^{\mathrm{s}} \boldsymbol{\eta}: \boldsymbol{\beta} \dot{T}\, \mathrm{d}\varOmega - \int_\varOmega \boldsymbol{\eta} \cdot \dot{\mathbf{b}} \mathrm{d}\varOmega - \int_{\varGamma_{\mathbf{t}}} \boldsymbol{\eta} \cdot \bar{\dot{\mathbf{t}}}\, \mathrm{d}\varGamma = 0 \\ &\qquad - \int_\varOmega \phi\, (\rho c)_{\mathrm{eff}}\, \dot{T}\, \mathrm{d}\varOmega + \int_\varOmega \nabla \phi \cdot \mathbf{q}_{\mathrm{T}} \mathrm{d}\varOmega + \int_{\varGamma_{q_{\mathrm{T}}}} \phi\, \bar{q}_{\mathrm{T}}\, \mathrm{d}\varGamma = 0 \end{aligned} \tag{43}$$

Using space discretization by introducing a discrete trial space $\mathcal{U}^h \times \mathcal{T}^h$ and testing space $\mathcal{U}^{\overset{h}{*}} \times \mathcal{T}^{\overset{h}{*}}$ corresponding to the chosen finite element interpolations, the fully discrete weak form of the problem is now

$$\begin{aligned} &\int_\varOmega \left(\nabla^s \boldsymbol{\eta}^h: \dot{\boldsymbol{\sigma}}''^h - \nabla^s \boldsymbol{\eta}^h: \boldsymbol{\beta} \dot{T}^h - \boldsymbol{\eta}^h \cdot \dot{\mathbf{b}}\right) \mathrm{d}\varOmega - \int_{\varGamma_t} \boldsymbol{\eta}^h \cdot \bar{\dot{\mathbf{t}}}\, \mathrm{d}\varGamma = 0 \\ &\quad \int_\varOmega \left(-\phi^h (\rho c)_{\mathrm{eff}} \dot{T}^h + \nabla \phi^h \cdot \mathbf{q}_{\mathrm{T}}^h\right) \mathrm{d}\varOmega + \int_{\varGamma_{q_{\mathrm{T}}}} \phi^h\, \bar{q}_{\mathrm{T}} \mathrm{d}\varGamma = 0 \end{aligned} \tag{44}$$

The displacement, pore pressure, and temperature fields are approximated as

$$\mathbf{u}^h = \mathbf{N}^d \mathbf{d}, \quad T^h = \mathbf{N}^{\mathrm{th}} \mathbf{T} \tag{45}$$

where $\mathbf{N}^d$, and $\mathbf{N}^{\mathrm{th}}$ are matrices of displacement and temperature shape functions, and $\mathbf{d}$ and $\mathbf{T}$ are the corresponding vectors of displacement and temperature unknowns. Furthermore, we define the following transformation matrices:

$$\begin{aligned} \nabla^s \mathbf{u}^h &= \mathbf{B} \mathbf{d} \\ \nabla T^h &= \mathbf{E}^{\mathrm{th}} \mathbf{T} \end{aligned} \tag{46}$$

Similarly, for temporal discretization, we use the generalized trapezoidal integration method and rewrite the balance of energy at a discrete time step n such that

$$\int_\varOmega - \phi^h (\rho c)_{\mathrm{eff}} \frac{T_{n+1}^h - T_n^h}{\Delta t} + \nabla \phi^h \cdot \mathbf{q}_{\mathrm{T}_{n+\theta}}^h + \int_{\varGamma_{q_{\mathrm{T}}}} \phi^h\, \bar{q}_{\mathrm{T}_{n+\theta}} \mathrm{d}\varGamma = 0 \tag{47}$$

where

$$\begin{aligned} \bar{q}_{\mathrm{T}_{n+\theta}} &= \theta \bar{q}_{\mathrm{T}_{n+1}} + (1 - \theta) \bar{q}_{\mathrm{T}_n} \\ \mathbf{q}_{\mathrm{T}_{n+\theta}} &= \theta \mathbf{q}_{\mathrm{T}_{n+1}} + (1 - \theta) \mathbf{q}_{\mathrm{T}_n} \end{aligned} \tag{48}$$

and $\theta \in [0,1]$ is an integration parameter. $\theta = 1$ gives the first-order backward-Euler scheme, and $\theta = 1/2$, gives the second-order Crank-Nicolson scheme. The incremental solution for the Newton-Raphson update at iteration $k + 1$ is determined as

$$\begin{bmatrix} \mathbf{K} & \boldsymbol{\Lambda} \\ \mathbf{0} & \mathbf{G} \end{bmatrix}_k \begin{bmatrix} \Delta \mathbf{d} \\ \Delta \mathbf{T} \end{bmatrix}_{(k+1)} = \begin{bmatrix} \mathbf{R}_G \\ \mathbf{R}_J \end{bmatrix}_k \tag{49}$$

where

$$\begin{aligned} \mathbf{K} &= \int_\varOmega \mathbf{B}^{\mathrm{T}}\, \bar{\mathbf{C}}_k \mathbf{B}\, \mathrm{d}\varOmega \\ \boldsymbol{\Lambda} &= - \int_\varOmega \mathbf{B}^{\mathrm{T}}\, \boldsymbol{\beta} \mathbf{N}^{\mathrm{th}}\, \mathrm{d}\varOmega \\ \mathbf{G} &= \theta \Delta t \int_\varOmega \mathbf{E}^{\mathrm{th}^{\mathrm{T}}}\, \bar{\mathbf{K}}_{\mathrm{T}_k} \mathbf{E}^{\mathrm{th}}\, \mathrm{d}\varOmega - \int_\varOmega \mathbf{N}^{\mathrm{th}^{\mathrm{T}}}\, \overline{(\rho c)_{\mathrm{eff}}} \mathbf{N}^{\mathrm{th}}\, \mathrm{d}\varOmega \end{aligned} \tag{50}$$

where $\bar{\mathbf{C}}$ and $\bar{\mathbf{K}}_{\mathrm{T}_k}$ are the homogenized consistent tangent and thermal conductivity tensors. The corresponding residual equations are

$$
\begin{aligned}
\mathbf{R}_G &= \int_\Omega \left(\nabla^s \boldsymbol{\eta}^h : \boldsymbol{\Sigma}_{n+1}^h - \boldsymbol{\eta}^h \cdot \mathbf{b}\right) \mathrm{d}\Omega - \int_{\Gamma_t} \boldsymbol{\eta}^h \cdot \bar{\mathbf{t}}_{n+1} \, \mathrm{d}\Gamma \\
\mathbf{R}_J &= \int_\Omega - \phi^h (\rho c)_{\mathrm{eff}} \frac{T_{n+1}^h - T_n^h}{\Delta t} + \nabla \phi^h \cdot \mathbf{Q}_{\mathrm{T}_{n+\theta}}^h + \int_{\Gamma_{q_\mathrm{T}}} \phi^h \, \bar{q}_{\mathrm{T}_{n+\theta}} \mathrm{d}\Gamma,
\end{aligned} \tag{51}
$$

Here, $\boldsymbol{\Sigma}_{n+1}^h$ and $\mathbf{Q}_{\mathrm{T}_{n+\theta}}^h$ are the homogenized macro stress at time step $n+1$ and homogenized macro flow at time step $n+\theta$.

Finally, the following material point update algorithm is implemented at each integration point of the Finite Element solver:

Input: $\mathbf{E}^n$, and $\mathbf{G}_\mathrm{T}^n$
Output: $\boldsymbol{\Sigma}^n$, $\bar{\mathbf{C}}^n$, $\mathbf{Q}_\mathrm{T}^n$, and $\bar{\mathbf{K}}_\mathrm{T}^n$

```
1.  Set local iteration counter $k = 0$ and initial guess $\mathbf{X}^k = 0$.
2.  For each layer $m \in L$:
        – Call solid material subroutine for layer $m$:
              Inputs: $\boldsymbol{\varepsilon}_m = \mathbf{E} + \mathbf{B}_1 \mathbf{v}_m, \ \boldsymbol{\varepsilon}_m^{n-1}$.
              Outputs: $\boldsymbol{\sigma}_m, \ \mathbf{C}_m$.
        – Call thermal subroutine for layer $m$:
              Inputs: $\nabla T_m = \mathbf{G}_\mathrm{T} + \mathbf{B}_2 g_{\mathrm{T}_m}, \ \nabla T_m^{n-1}$.
              Outputs: $\mathbf{q}_{\mathrm{T}_m}, \ \boldsymbol{\kappa}_{\mathrm{T}_m}$.
3.  Assemble residual $\mathbf{R}^k(\mathbf{X}^k)$.
4.  If $\| \mathbf{R}^k \| < \varepsilon_{\mathrm{tol}}$ go to Step 7.
5.  Else, perform Newton update $\mathbf{X}^{k+1} = \mathbf{X}^k - (\mathbf{J}^{-1})^k \, \mathbf{R}^k$.
6.  Set $k \leftarrow k + 1$ and return to Step 2.
7.  Compute the macro-stress $\boldsymbol{\Sigma} = \sum_{m \in L} \phi_m \, \boldsymbol{\sigma}_m$.
8.  Compute the macro-flux $\mathbf{Q}_\mathrm{T} = \sum_{m \in L} \phi_m \, \mathbf{q}_{\mathrm{T}_m}$.
9.  Compute the consistent tangent operator $\bar{\mathbf{C}}^n$,
    and macroscopic heat conductivity matrix $\bar{\mathbf{K}}_\mathrm{T}^n$.
10. Save the sub-model states of each layer for the next timestep:
        – $\boldsymbol{\varepsilon}_m^n \leftarrow \boldsymbol{\varepsilon}_m$.
        – $\nabla T_m^n \leftarrow \nabla T_m$.
```

4. RESULTS AND DISCUSSION

In this section, we present several numerical examples using the proposed multiscale modeling framework to assess its performance in capturing the thermo-mechanical response of rocks. This includes anisotropy in mechanical and thermal properties. We will incorporate different constitutive laws for the layers at the microscopic scale to demonstrate the flexibility of the framework.

4.1 Micro-constitutive Models

For a linear elastic material, the stress tensor of the layers is related to the strain tensor of the layers as

$$
\boldsymbol{\sigma} = \mathbb{C}^\mathrm{e} : \boldsymbol{\varepsilon} \,, \quad \mathbb{C}^\mathrm{e} = \mathrm{K}(\mathbf{1} \otimes \mathbf{1}) + 2\mathrm{G}\left(-\tfrac{1}{3} \mathbf{1} \otimes \mathbf{1}\right) \tag{52}
$$

in which K and G denote the bulk and shear moduli, respectively. The elasto-plastic model considered is the Modified Cam-Clay (MCC) model, with the following yield function:

$$
f(p, q, p_c) = \frac{q^2}{M^2} + p(p - p_c) \leq 0 \tag{53}
$$

where $M > 0$ is the slope of the critical state line (CSL), and $p_c > 0$ is the pre-consolidation pressure. p and q are the volumetric and deviatoric stress invariants, respectively, which are defined as

$$
p := \frac{1}{3} \mathrm{tr}(\boldsymbol{\sigma}), \quad q := \sqrt{\frac{3}{2}} \| \boldsymbol{\sigma} - p \mathbf{1} \| \tag{54}
$$

The hardening law is given by

$$
\dot{p}_c = h \, \mathrm{tr}(\dot{\boldsymbol{\varepsilon}}^\mathrm{p}) \tag{55}
$$

In which $\mathrm{tr}(.)$ Denotes the trace of a tensor and h is the hardening modulus.

4.2 Example 1: Comparison of the Homogenized and High-fidelity Models

This example demonstrates the performance of the proposed model for general initial-boundary value problems. For this purpose, we simulate a time-dependent, anisotropic thermo-mechanical plane strain problem for consolidation of a layered thermo-elastic column of height L and width L. The domain consists of 20 layers of equal size (alternating as layer A and layer B), with a constant distributed load w and a constant heat flux applied on the top. The lower boundary is fixed in the vertical direction, with its midpoint also fixed in the horizontal direction. The column is discretized uniformly into 20 quadrilateral elements with biquadratic displacement and bilinear temperature. The prescribed distributed load is $w = -1 \times 10^5$ Pa and the prescribed heat flux is $1.59 \ \mathrm{W}/m^2$. The material properties selected for the layers are shown in Table 1. Using the standard displacement-based finite element method in conjunction with Newton's method, we solve this problem with a constant time increment of 1 day. The deal.II Finite Element Library is used for the finite element simulations.

We once simulate this problem by explicitly modeling the individual layers (shown with label "direct" in Figures 1 and 2), and once with the proposed homogenization approach in which a two-layer unit cell consisting of layer A and layer B is used (shown with label "homogenized" in Figures 1 and 2). We observe from Figures 1 and 2 that the homogenization approach captures the overall responses of the layers well. The homogenized strain and temperature gradient align exactly with the direct responses and reflect the variation in strain and temperature gradient in layers A and B. Figure 2 verifies that the stresses in layers A and B are in equilibrium with the macroscopic applied stress.

Table 1: Simulation parameters used in Example 1.

Properties	E (Pa)	ν	ρ (kg/m^3)	C_p (J/kg/°C)	α_s(1/°C)	κ (W/m/°C)
Layer A	40×10^9	0.25	2000	1000	5×10^{-6}	2
Layer B	75×10^9	0.25	2000	1000	5×10^{-6}	4

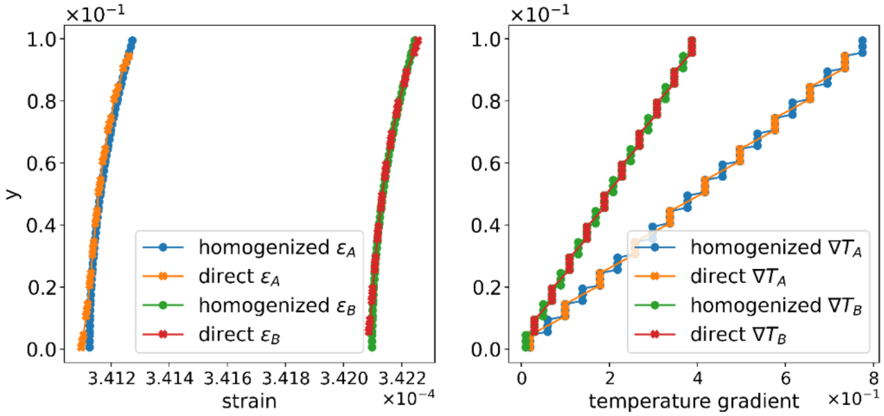

Figure 1: Results of explicit modeling of layers (labeled as "direct") and homogenization model results for strain and temperature gradient at the integration points along the vertical direction for layers A and B.

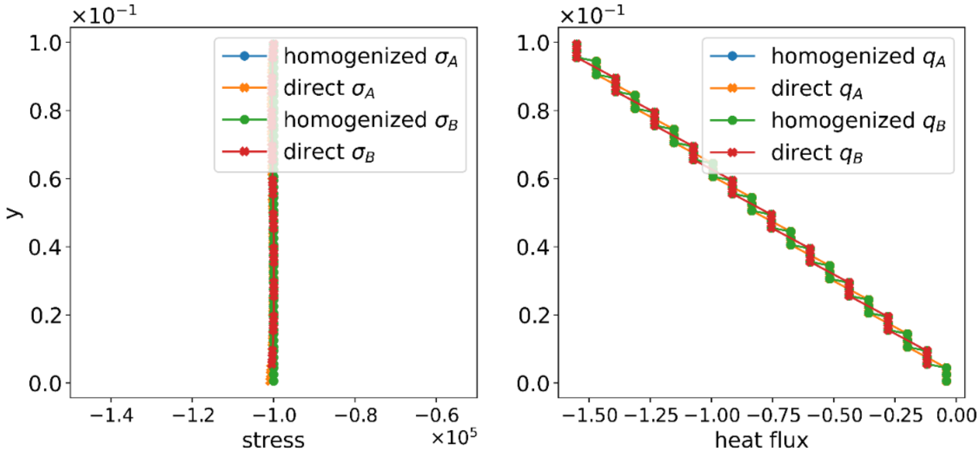

Figure 2: Results of explicit modeling of layers (labeled as "direct") and homogenization model results for stress and heat flux gradient at the integration points along the vertical direction for layers A and B.

4.3 Example 2: Borehole Problem

This example aims to investigate the performance of the homogenization model in simulating boundary value problems. For this purpose, the thermo-mechanical material point update algorithm is implemented within each integration point of a nonlinear finite element solver to simulate the anisotropic response. Specifically, we study the performance of the homogenization model in the application of time-dependent behavior of boreholes in anisotropic rocks, which is relevant for wellbore stability.

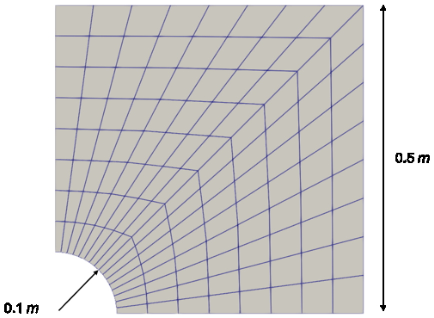

Figure 3: The geometry and mesh used for the borehole problem in Example 2.

We consider a borehole with a radius of 0.1 m represented in 2D as a circle inside a square domain in plane strain conditions (Figure 3). The dimension of the model is 1 m by 1 m in the x and y directions. Due to symmetry, only a quarter of the geometry is simulated. In this case, all external boundaries have a roller support and zero flux boundary conditions, while the borehole surface is subjected to radial traction and heat flux. The domain consists of Haynesville shale material with properties shown in Table 2. The mechanical properties are based on the parameters calibrated by Choo et al. (2021). The initial rock temperature is assumed as 0℃. Using the standard displacement-based finite element method, we simulate the domain using quadrilateral elements with biquadratic displacement and bilinear temperature at a constant time increment of 0.5 day. To examine the effect of anisotropy on the borehole behavior, we repeat the simulations with three different bedding plane orientations of $\theta = 0°$, $\theta = 45°$, and $\theta = 90°$.

Table 2: Simulation parameters used in Example 2 for anisotropic Haynesville shale.

Property	ϕ	E (Pa)	ν	M	p_c(Pa)	h (Pa)	ρ (kg/m^3)	C_p (J/kg/°C)	α_s(1/°C)	κ(W/m/°C)
Layer A	0.455	5.9×10^9	0.28	0.9	18×10^6	225×10^2	2366	1004	11.39×10^{-6}	1.8
Layer B	0.545	41×10^9	0.36	-	-	-	2366	1004	11.39×10^{-6}	5.8

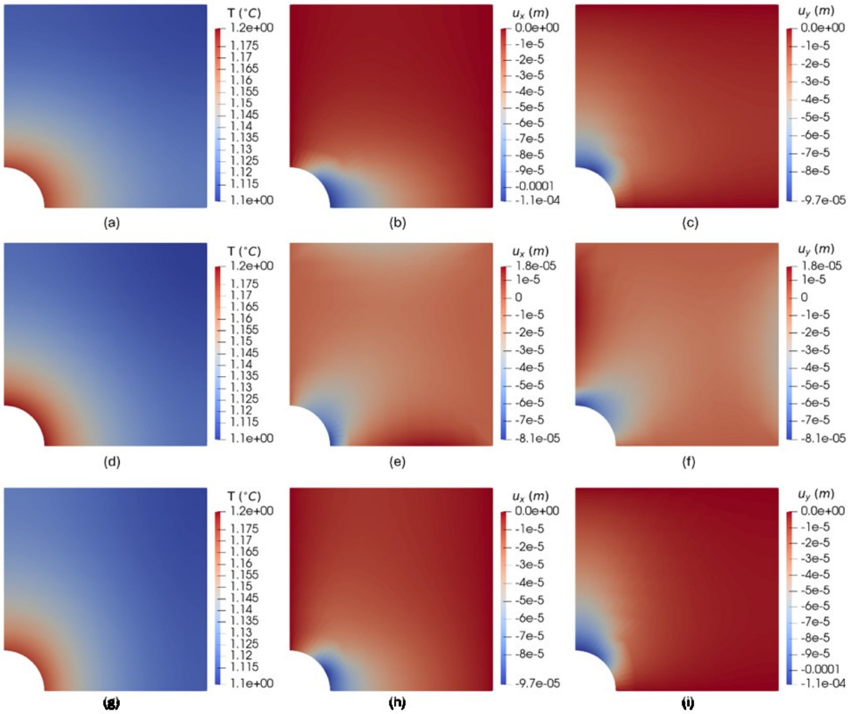

Figure 4: Temperature and displacement responses for (a-c) $\boldsymbol{\theta = 0°}$, (d-f) $\boldsymbol{\theta = 45°}$, and (g-i) $\boldsymbol{\theta = 90°}$

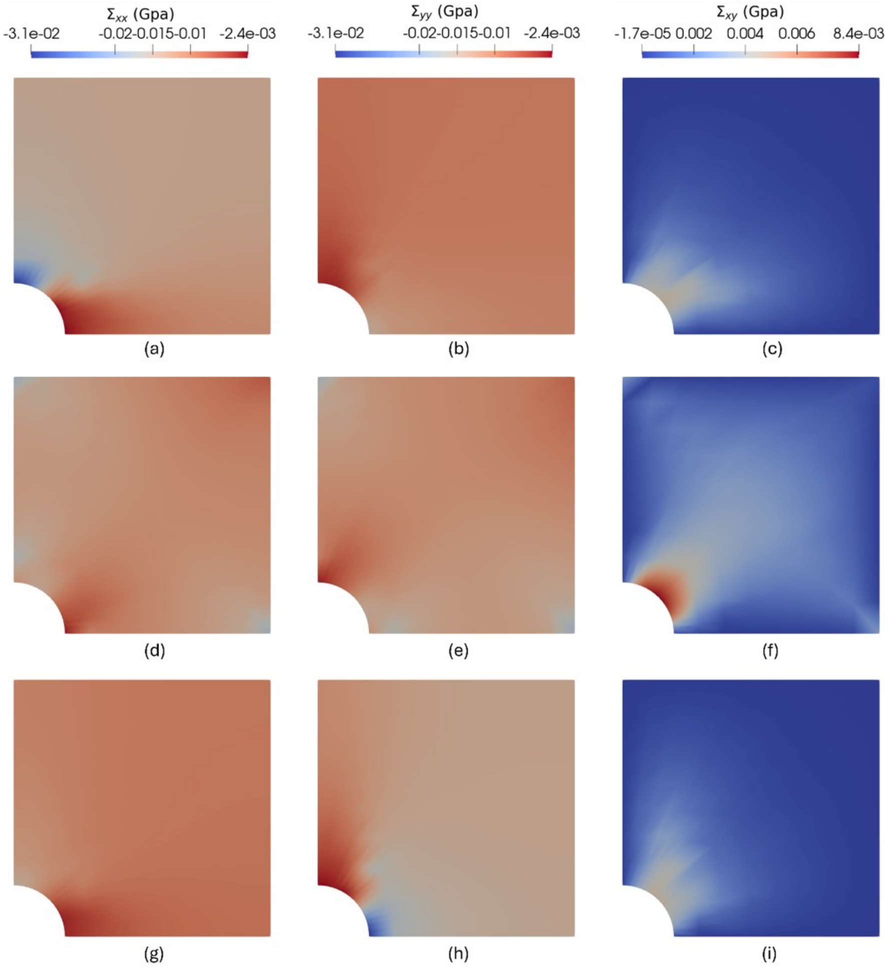

(a) (b) (c)

(d) (e) (f)

(g) (h) (i)

Figure 5: Macroscopic stress responses for (a-c) $\theta = 0°$, (d-f) $\theta = 45°$, and (g-i) $\theta = 90°$

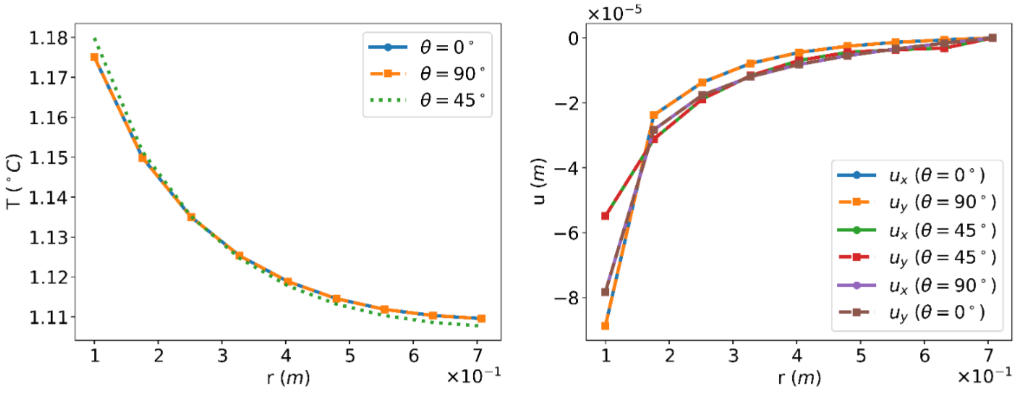

(a) (b)

Figure 6: Temperature (a) and displacement (b) variations in the radial direction for three bedding plane angles.

The results are shown in Figures 4 to 6. It is observed that the x and y displacement responses (Figure 4) as well as the macroscopic stresses Σ_{xx}, Σ_{yy} and Σ_{xy} are dependent on the bedding plane angle, where the x and y displacement and stresses between $\theta = 0°$ and $\theta = 90°$ are mirrors of each other around the diagonal axis, as expected due to symmetry. Similarly, we observe in Figure 6(b) that u_x at $\theta = 0°$ is the same as u_y at $\theta = 90°$ and vice versa. Figure 6(a) shows that the variation of temperature in the radial direction is the same for $\theta = 0°$ and $\theta = 90°$, while it is different for $\theta = 45°$. Bedding plane orientation of $\theta = 45°$ leads to the largest magnitude of shear stress in the domain.

5. CONCLUSION

Accurately representing anisotropy of rocks in geothermal applications is challenging because anisotropy can be scale-dependent, where direct discretization of all layers is typically infeasible. Homogenization and multiscale methods provide a systematic approach to derive effective macroscale constitutive behavior from an explicit description of the microscale. This work develops a thermo-mechanical homogenization framework tailored to layered geomaterials relevant to EGS applications. By constructing effective thermo-mechanical properties from microstructural descriptions, our homogenization model avoids the expensive cost of using fine mesh in field-scale finite element simulations.

REFERENCES

Abuel-Naga, H. M., & Bergado, D. T. (2005). Thermal conductivity and fabric anisotropy of saturated clays. Geotechnical Engineering Journal (Journal of the Southeast Asian Geotechnical Society), 36(2), 99–108.

Aliyu, M. D. (2025). Advanced 3D thermo-hydro-mechanical modelling of thermal aperture evolution in enhanced geothermal systems. Energy Conversion and Management, 342, 120129. https://doi.org/10.1016/j.enconman.2025.120129

Chen, J., Liu, S., Shen, W., Shao, J., & Vu, M.-N. (2023). Enhancing the elastoplastic damage constitutive model for clayey rocks: Incorporating anisotropy, saturation, time-dependent, and debonding effects. Journal of Rock Mechanics and Geotechnical Engineering, 15(9), 2291–2312. https://doi.org/10.1016/j.jrmge.2023.05.013

Choo, J., Semnani, S. J., & White, J. A. (2021). An anisotropic viscoplasticity model for shale based on layered microstructure homogenization. International Journal for Numerical and Analytical Methods in Geomechanics, 45(4), 502–520. https://doi.org/10.1002/nag.3167

Cooper, H. W., & Simmons, G. (1977). The effect of cracks on the thermal expansion of rocks. Earth and Planetary Science Letters, 36(3), 404–412. https://doi.org/10.1016/0012-821X(77)90065-6

Dafalias, Y. F., Manzari, M. T., & Papadimitriou, A. G. (2006). SANICLAY: Simple anisotropic clay plasticity model. International Journal for Numerical and Analytical Methods in Geomechanics, 30(12), 1231–1257. https://doi.org/10.1002/nag.524

Davis, M. G., Chapman, D. S., Van Wagoner, T. M., & Armstrong, P. A. (2007). Thermal conductivity anisotropy of metasedimentary and igneous rocks. Journal of Geophysical Research: Solid Earth, 112(B5), B05216. https://doi.org/10.1029/2006JB004755

Giraud, A., Gruescu, C., Do, D. P., Homand, F., & Kondo, D. (2007). Effective thermal conductivity of transversely isotropic media with arbitrary oriented ellipsoïdal inhomogeneities. International Journal of Solids and Structures, 44(9), 2627–2647. https://doi.org/10.1016/j.ijsolstr.2006.08.011

Giraud, A., Hoxha, D., Do, D. P., & Magnenet, V. (2008). Effect of pore shape on effective porothermoelastic properties of isotropic rocks. International Journal of Solids and Structures, 45, 1–23. https://doi.org/10.1016/j.ijsolstr.2007.07.005

Jiménez-Camargo, J. A., Blanco-Martín, L., Rouabhi, A., & Hadj-Hassen, F. (2025). Effects of stress extrapolation and dilatancy on salt cavern design: An application to underground hydrogen storage. Rock Mechanics and Rock Engineering. Advance online publication. https://doi.org/10.1007/s00603-025-04897-8

Kim, H., Cho, J.-W., Song, I., & Min, K.-B. (2012). Anisotropy of elastic moduli, P-wave velocities, and thermal conductivities of Asan gneiss, Boryeong shale, and Yeoncheon schist in Korea. Engineering Geology, 147–148, 68–77. https://doi.org/10.1016/j.enggeo.2012.07.015

Pandey, S. N., Chaudhuri, A., & Kelkar, S. (2017). A coupled thermo-hydro-mechanical modeling of fracture aperture alteration and reservoir deformation during heat extraction from a geothermal reservoir. Geothermics, 65, 17–31. https://doi.org/10.1016/j.geothermics.2016.08.006

Parisio, F., Vilarrasa, V., Wang, W., Kolditz, O., & Nagel, T. (2019). The risks of long-term re-injection in supercritical geothermal systems. Nature Communications, 10, Article 4391. https://doi.org/10.1038/s41467-019-12146-0

Rathnaweera, T. D., Wu, W., Ji, Y., & Gamage, R. P. (2020). Understanding injection-induced seismicity in enhanced geothermal systems: From the coupled thermo-hydro-mechanical-chemical process to anthropogenic earthquake prediction. Earth-Science Reviews, 205, 103182. https://doi.org/10.1016/j.earscirev.2020.103182

Rezania, M., & Dejaloud, H. (2021). BS-CLAY1: Anisotropic bounding surface constitutive model for natural clays. Computers and Geotechnics, 135, 104099. https://doi.org/10.1016/j.compgeo.2021.104099

Salimzadeh, S., Paluszny, A., Nick, H. M., & Zimmerman, R. W. (2018). A three-dimensional coupled thermo-hydro-mechanical model for deformable fractured geothermal systems. Geothermics, 71, 212–224. https://doi.org/10.1016/j.geothermics.2017.09.012

Semnani, S. J., White, J. A., & Borja, R. I. (2016). Thermoplasticity and strain localization in transversely isotropic materials based on anisotropic critical state plasticity. *International Journal for Numerical and Analytical Methods in Geomechanics*, *40*(18), 2423-2449.

Semnani, S. J., & White, J. A. (2020). An inelastic homogenization framework for layered materials with planes of weakness. Computer Methods in Applied Mechanics and Engineering, 370, 113221. https://doi.org/10.1016/j.cma.2020.113221

Tester, J. W., Anderson, B. J., Batchelor, A. S., Blackwell, D. D., DiPippo, R., Drake, E. M., Garnish, J., Livesay, B., Moore, M. C., Nichols, K., Petty, S., Toksöz, M. N., & Veatch, R. W. (2006). The future of geothermal energy: Impact of enhanced geothermal systems (EGS) on the United States in the 21st century (Technical Report No. INL/EXT-06-11746). Massachusetts Institute of Technology. https://energy.mit.edu/wp-content/uploads/2006/11/MITEI-The-Future-of-Geothermal-Energy.pdf

Vaezi, I., Yoshioka, K., De Simone, S., Gómez-Castro, B. M., Paluszny, A., Jalali, M., Berre, I., Rutqvist, J., Min, K.-B., Lei, Q., Makhnenko, R. Y., Hu, M., Tsang, C.-F., & Vilarrasa, V. (2025). A review of thermo-hydro-mechanical modeling of coupled processes in fractured rock: From continuum to discontinuum perspective. Journal of Rock Mechanics and Geotechnical Engineering, 17(11), 7460–7488. https://doi.org/10.1016/j.jrmge.2025.04.033

Wang, Y., Wang, Z., Shi, L., Rong, Y., Hu, J., Jiang, G., Wang, Y., & Hu, S. (2021). Anisotropic differences in the thermal conductivity of rocks: A summary from core measurement data in East China. Minerals, 11(10), 1135. https://doi.org/10.3390/min11101135

Wheeler, S. J., Näätänen, A., Karstunen, M., & Lojander, M. (2003). An anisotropic elastoplastic model for soft clays. Canadian Geotechnical Journal, 40(2), 403–418. https://doi.org/10.1139/T02-119

Wu, S., Yu, Z., Kang, J., Zhang, Y., & Gao, P. (2021). Research on the anisotropy of thermal conductivity of rocks in Songliao Basin, China. Renewable Energy, 179, 593–603. https://doi.org/10.1016/j.renene.2021.06.113

Yin, Z.-Y., Chang, C. S., Karstunen, M., & Hicher, P.-Y. (2010). An anisotropic elastic–viscoplastic model for soft clays. International Journal of Solids and Structures, 47(5), 665–677. https://doi.org/10.1016/j.ijsolstr.2009.11.004

Zhou, D., Tatomir, A., Liu, Q., Li, K., Gao, H., & Sauter, M. (2024). Effects of thermoelasticity induced aperture variation on performances of enhanced geothermal system. Applied Thermal Engineering, 248, 123308. https://doi.org/10.1016/j.applthermaleng.2024.123308

Zhou, W., Lanza, F., Grigoratos, I., Schultz, R., Cousse, J., Trutnevyte, E., Muntendam-Bos, A., & Wiemer, S. (2024). Managing induced seismicity risks from enhanced geothermal systems: A good practice guideline. Reviews of Geophysics, 62(4), e2024RG000849. https://doi.org/10.1029/2024RG000849